

PARTICLE ACCELERATION AND WAVE EXCITATION IN QUASI-PARALLEL HIGH-MACH-NUMBER COLLISIONLESS SHOCKS: PARTICLE-IN-CELL SIMULATION

TSUNEHICO N. KATO¹

Department of Physical Science, Graduate School of Science, Hiroshima University and
1-3-1, Kagamiyama, Higashi-Hiroshima, Hiroshima 739-8526, Japan

Draft version July 9, 2018

ABSTRACT

We herein investigate shock formation and particle acceleration processes for both protons and electrons in a quasi-parallel high-Mach-number collisionless shock through a long-term, large-scale particle-in-cell simulation. We show that both protons and electrons are accelerated in the shock and that these accelerated particles generate large-amplitude Alfvénic waves in the upstream region of the shock. After the upstream waves have grown sufficiently, the local structure of the collisionless shock becomes substantially similar to that of a quasi-perpendicular shock due to the large transverse magnetic field of the waves. A fraction of protons are accelerated in the shock with a power-law-like energy distribution. The rate of proton injection to the acceleration process is approximately constant, and in the injection process, the phase-trapping mechanism for the protons by the upstream waves can play an important role. The dominant acceleration process is a Fermi-like process through repeated shock crossings of the protons. This process is a ‘fast’ process in the sense that the time required for most of the accelerated protons to complete one cycle of the acceleration process is much shorter than the diffusion time. A fraction of the electrons is also accelerated by the same mechanism, and have a power-law-like energy distribution. However, the injection does not enter a steady state during the simulation, which may be related to the intermittent activity of the upstream waves. Upstream of the shock, a fraction of the electrons is pre-accelerated before reaching the shock, which may contribute to steady electron injection at a later time.

Subject headings: acceleration of particles – cosmic rays – ISM: supernova remnants – methods: numerical – plasmas – shock waves

1. INTRODUCTION

Collisionless shocks, which are driven by various violent phenomena throughout the universe, are believed to be sites of particle acceleration. In particular, cosmic rays with energies below the knee energy (approximately $10^{15.5}$ eV) are considered to be accelerated by shocks in supernova remnants (SNRs) in our galaxy. A number of X-ray observations have revealed synchrotron X-rays radiated from high-energy electrons around the shocks in several young SNRs, and these synchrotron X-rays are regarded as evidence of electron acceleration around the shocks to energies of approximately 10^{14} eV (Koyama et al. 1995; Long et al. 2003; Bamba et al. 2003). Recent observations have also revealed gamma rays associated with the decay of neutral pions (π^0 mesons), which occurs as a result of proton-proton collisions (Ackermann et al. 2013). These observations are regarded as direct evidence of high-energy protons in the vicinity of the shocks.

One of the most plausible candidates for the acceleration process that acts in shocks is first-order Fermi acceleration (Drury 1983; Blandford & Eichler 1987). In particular, first-order Fermi acceleration can explain the power-law energy spectrum for the accelerated particles and the power-law index expected from the observations of cosmic rays. However, the acceleration process that is

actually operating in the SNR shocks has not yet been determined, especially with respect to electron acceleration, and further observational and theoretical investigations are needed.

Generally, it is considered that the acceleration efficiency is strongly dependent on the shock velocity or the shock Mach number, and the process would be more efficient for larger velocity or higher Mach number shocks. For example, young SNRs have large shock velocities (approximately 1,000 to 10,000 km s⁻¹), and the corresponding Mach number is very large (approximately 100). Young SNRs are believed to be efficient accelerators of particles. In addition, the orientation of the background magnetic field upstream of the shock can also have a significant influence on the efficiency of the particle acceleration process. For example, the bipolar morphology of the emission region of non-thermal synchrotron X-rays in the supernova remnant SN1006 is considered to be related to the orientation of the magnetic field in the interstellar medium around the remnant, which is upstream of the shock. Recent observations of radio polarization by Reynoso et al. (2013) suggest that the electron acceleration is efficient when the direction of the ambient magnetic field is approximately parallel to the shock normal. Hence, the particle acceleration process can be more efficient in quasi-parallel shocks than in quasi-perpendicular shocks. Here, shocks in which the upstream magnetic field lies along the shock normal are referred to as parallel shocks, and shocks in which the upstream field lies perpendicular to the shock normal are referred to as perpendicular shocks.

tsunehiko.kato@nao.ac.jp

¹Current address: Center for Computational Astrophysics, National Astronomical Observatory of Japan, 2-21-1 Osawa, Mitaka, Tokyo 181-8588, Japan

In the heliosphere, collisionless shocks (e.g., Earth’s bow shock, interplanetary shocks associated with coronal mass ejections, solar wind termination shocks, etc.) are also formed. These shocks have been investigated through a number of direct *in situ* observations by spacecraft: For example, the Earth’s bow shock (Burgess et al. 2012) and those associated with solar energetic particles and energetic storm particle events (Lee et al. 2012). In particular, these observations indeed showed that quasi-parallel shocks can be efficient ion accelerators and their efficiency is generally dependent on the shock strength (Reames 2000). The wave generation in the upstream region of shocks by reflected energetic diffuse ions are also observed in Earth’s bow shock (Hoppe et al. 1981; Burgess et al. 2005). Although the Alfvén Mach numbers of these shocks are generally smaller than those of SNR shocks, recently, a quasi-parallel collisionless shock at very high Mach number of ~ 100 have been observed in Saturn’s bow shock by Cassini spacecraft (Masters et al. 2013). This observation also showed an efficient electron acceleration there, suggesting that quasi-parallel shocks at very high Mach numbers can be efficient electron accelerators, too.

The acceleration processes in shocks have also been investigated through numerical simulations. Recent large-scale hybrid simulations, in which protons are treated as discrete particles whereas electrons are approximated as a massless fluid, have shown that protons are accelerated efficiently in quasi-parallel shocks with a power-law-like energy distribution (Giacalone 2004; Sugiyama 2011; Gargatè & Spitkovsky 2012; Caprioli & Spitkovsky 2014). The acceleration process observed in these studies is often a ‘fast’ process in the sense that the accelerated protons cross the shock front back and forth repeatedly within a much shorter timescale than that of the diffusive motion. Another prominent feature of these particle accelerating shocks is the wave excitation in the upstream region of the shock by the accelerated protons, which would be a similar processes to those observed in quasi-parallel Earth’s bow shocks by *in situ* observations. The amplitude of these waves can be even larger than the strength of the background magnetic field. These large-amplitude upstream waves can strongly influence both the particle acceleration process and the shock structure.

Hybrid simulations, however, cannot deal with the kinetic dynamics of electrons, especially non-thermal electron acceleration. In the present paper, we investigate the particle acceleration process for both protons and electrons in high-Mach-number quasi-parallel shocks, as well as the shock formation process and structure, taking into account the electron dynamics self-consistently through particle-in-cell (PIC) simulations in which both protons and electrons are treated as discrete particles. For protons to be accelerated to sufficiently high energies, long-term (typically hundreds of proton gyro-time) and therefore large-scale simulations are required. In order for the calculation time to be as long as possible, we carry out a large-scale one-dimensional simulation. In Section 2, we describe the simulation model. The primary results of the simulation are shown in Section 3. The obtained results are discussed in Section 4, and conclusions are presented in Section 5.

2. METHOD

In order to investigate the particle acceleration process in quasi-parallel collisionless shocks in an electron-proton plasma, we carry out a large-scale numerical simulation. The simulation code is a one-dimensional electromagnetic particle-in-cell code with one spatial dimension and three velocity dimensions (1D3V) that was developed based on a standard method described by Birdsall & Langdon (1991). The basic equations are the Maxwell’s equations and the (relativistic) equation of motion of particles. In the following, we take the x -axis as the one-dimensional direction.

In the simulation, a collisionless shock is driven according to the ‘injection method’. There are two conducting rigid walls at both ends of the simulation box. These walls reflect both incident particles and electromagnetic waves specularly. Initially, the plasma is moving in the $+x$ -direction at a bulk velocity V . Both electrons and protons are loaded uniformly in the region between the two walls with an average velocity of V plus the thermal velocity, where the temperatures of the electrons and protons are initially set to be equal. As the plasma is magnetized, the plasma convects the ordered background magnetic field \mathbf{B}_0 . Since the electric field should vanish in the plasma rest frame, the motional electric field $\mathbf{E}_0 = -\mathbf{V} \times \mathbf{B}_0$ appears in the simulation frame, in which the plasma is moving. In the early stage of the simulation, the particles that collide with the wall on the $+x$ side are reflected specularly and then interact with the incoming plasma. This interaction causes some instabilities and eventually leads to the formation of a collisionless shock. The frame of the simulation is the rest frame of the shock downstream plasma (hereinafter, the downstream rest frame). Thus, in the simulation, we observe the propagation of the collisionless shock in the $-x$ -direction in the downstream rest frame.

In the following, we take ω_{pe}^{-1} as the unit of time and $\lambda_e = c\omega_{pe}^{-1}$ as the unit of length, where $\omega_{pe} = (4\pi n_{e0}e^2/m_e)^{1/2}$ is the electron plasma frequency defined for the far upstream plasma number density n_{e0} with electron mass m_e and magnitude of the electron charge $e = |e|$. The units of the electric and magnetic fields are given by $E_* = B_* = c(4\pi n_{e0}m_e)^{1/2}$.

3. RESULTS

We carry out a large-scale one-dimensional PIC simulation under the following conditions. We use a reduced proton mass of $m_p = 30m_e$ for which the proton inertial length is given by $\lambda_p = 5.48\lambda_e$. The number of spatial grids is $N_x = 2.5 \times 10^6$, and there are $N_{\text{PPC}} = 160$ super-particles per cell per species. The physical dimension of the simulation box is $L_x = 1.5 \times 10^5 \lambda_e = 2.74 \times 10^4 \lambda_p$. The size of a cell is thus $\Delta x = 0.06\lambda_e$. The time step is taken to be $\Delta t = 0.05\omega_{pe}^{-1}$.

The initial bulk velocity of the plasma is given by $V = 0.37c$ in the $+x$ -direction. The corresponding Lorentz factor is given by $\Gamma = 1.08$, and thus the relativistic effect is not significant for the shock formation. The ordered background magnetic field is set on the x - y plane, and, in order to study a quasi-parallel shock, the angle between it and the x -axis (i.e., the shock normal) is taken to be $\Theta_0 = 30^\circ$ in the downstream rest frame. Hence, the motional electric field lies in the $-z$ -direction. The strength of the background magnetic field $B_0 = |\mathbf{B}_0|$ is

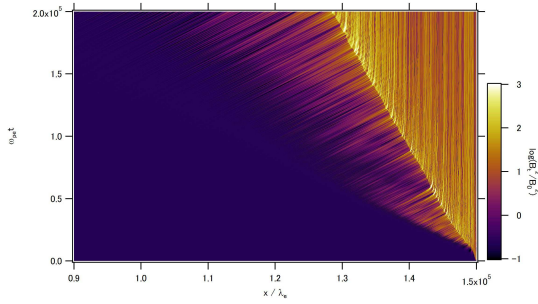


Figure 1. Time evolution of the energy density of the transverse magnetic field $B_t = (B_y^2 + B_z^2)^{1/2}$. The horizontal and vertical axes indicate the x -coordinate and the time, respectively. The value of $\log_{10}(B_t^2/B_0^2)$ is shown in grayscale (color). A collisionless shock is formed on the right-hand side and propagates to the left. Large-amplitude ($B_t \gg B_0$) waves are evident upstream (left-hand side) of the shock.

set so that $B_0/B_* = \omega_{ce}/\omega_{pe} = 8.847 \times 10^{-2}$, where $\omega_{ce} = eB_0/m_e c$ is the electron cyclotron frequency. The proton gyro frequency is given by $\omega_{cp} = 2.95 \times 10^{-3} \omega_{pe}$. The Alfvén velocity in the upstream region is thus given by $v_A = 1.59 \times 10^{-2} c$. In terms of the magnetization, $\sigma \equiv B_0^2/4\pi n_{e0}(m_e + m_p)V^2$, which corresponds to $\sigma = 1.9 \times 10^{-3}$, i.e., it is very weakly magnetized. The plasma beta parameters defined for electrons and protons are both set to be 0.5, so that the total plasma beta becomes unity ($\beta = \beta_e + \beta_p = 1$) and the initial temperatures of electrons and protons are determined accordingly ($T_e = T_p = 1.96 \times 10^{-3} m_e c^2$).

3.1. Structure of Collisionless Shock

Figure 1 presents the evolution of the magnetic energy density of the transverse components, $B_t = (B_y^2 + B_z^2)^{1/2}$, normalized by that of the background field $B_0^2/8\pi$. A collisionless shock is observed to form in the vicinity of the wall located at $x = 1.5 \times 10^5 \lambda_e$ and then propagate to the left at an approximately constant speed. The shock speed is obtained as approximately $-0.1c$ in the downstream rest frame (namely, the simulation frame) and approximately $-0.46c$ in the upstream rest frame. The corresponding Alfvén Mach-number is given by $M_A \sim 28$. (Note that although this Mach number would be generally regarded as ‘high’ Mach number, it is still small compared with the typical values for SNR shocks $M_A \sim 100$.) It is also evident in this figure that there exist large-amplitude ($B_t \gg B_0$) waves in the upstream region (left-hand side) of the shock. These waves appear around $\omega_{pe} t \sim 1.5 \times 10^4$, and the region in which they exist, which is sometimes referred to as the foreshock region, extends upstream with time. This excitation of the waves in the upstream region can be attributed to the appearance of the energetic particles (Bell 1978). Indeed, excitation is commonly observed in numerical simulations in which a fraction of the particles is accelerated in the shock efficiently under the quasi-parallel condition, for example, in non-relativistic hybrid simulations (Giacalone 2004; Caprioli & Spitkovsky 2014) and relativistic PIC simulations (Sironi & Spitkovsky 2011).

Figure 2(a) shows the profiles of the magnetic field components B_y and B_z around the shock at $\omega_{pe} t = 1 \times 10^5$, where the shock front is located at $x \sim 1.3886 \times$

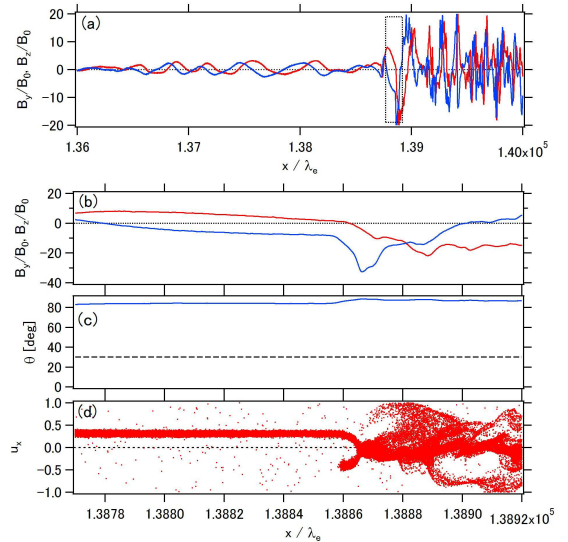


Figure 2. (a) Magnetic fields B_y (black) and B_z (red) around the shock at $\omega_{pe} t = 1 \times 10^5$ normalized by the background field B_0 . (b) Close-up of the region enclosed by the dotted box in (a). (c) Angle of the local magnetic field to the shock normal (x -axis). (d) $x - u_x$ phase-space plot of the protons, where u_x denotes the x -component of the particle 4-velocity.

$10^5 \lambda_e$. Large-amplitude waves occur upstream of the shock, and the magnetic fields of the waves are much larger than the background field B_0 in the vicinity of the shock. Figure 2(b) shows a close-up of the region indicated by the dotted box in Fig. 2(a). The transverse magnetic fields are dominant around the shock. As shown in Fig. 2(c), the local magnetic field and the shock normal (i.e., the x -axis) are approximately perpendicular. Since the shock structure is much smaller than the typical wavelength of the upstream waves, the shock experiences an almost uniform perpendicular magnetic field. Therefore, the local shock structure itself becomes essentially that of the *quasi-perpendicular* shock. Indeed, Fig. 2(d) shows that some of the incoming upstream protons are reflected at the shock front, which is a well-known characteristic of quasi-perpendicular shocks. Due to this strong perpendicular magnetic field, the local Alfvén Mach number becomes $M_A \sim 3.6$. Thus, the shock itself is locally not a high-Mach-number shock.

3.2. Wave Excitation in the Upstream Region

Figure 3(a) shows the profiles of the magnetic field around the shock, as in Fig. 2(a). Figure 3(b) shows a close-up of the region $1.32 \times 10^5 < x/\lambda_e < 1.35 \times 10^5$ indicated by the dotted box in Fig. 3(a) together with the electric fields. The generated waves are monochromatic rather than turbulent, as is clear from the figure. The wavelengths of these waves are typically $\lambda \sim 200\lambda_e - 400\lambda_e$, which is comparable to or somewhat larger than the gyro-radius of the protons reflected at the shock (defined for the background field strength B_0). The wavelength satisfies the condition $\lambda \gg 2\pi v_A/\omega_{cp} \sim 34\lambda_e$, where $\omega_{cp} = eB_0/m_p c$ is the cyclotron frequency of the upstream protons, and so are regarded as Alfvénic electromagnetic waves. Although the waves actually propagate obliquely with respect to the background field, the structures of the electric and magnetic fields of the waves are essentially the same as the structure of right-hand

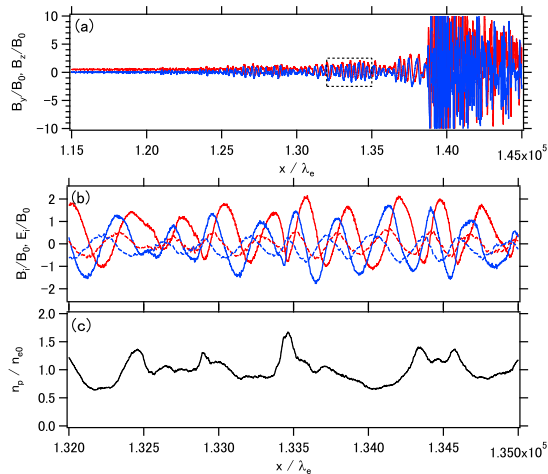


Figure 3. (a) Magnetic fields around the shock at $\omega_{pe}t = 1 \times 10^5$, as in Fig. 2(a). (b) Close-up of the region enclosed by the dotted box in (a). The normalized electric fields E_y/B_0 and E_z/B_0 are also shown by the dashed curves. (c) Number density of protons n_p normalized by the number density far upstream n_{e0} .

circularly polarized waves and are naturally explained to be generated by the resonant mode instability (Winske & Leroy 1984). The number density of the incoming upstream plasma is also modulated because of the existence of the waves, as shown in Fig. 3(c). This compressive behavior can be explained as a non-linear effect or a feature of obliquely propagating unstable modes (Gary et al. 1981).

Figure 4 shows the features of the upstream waves observed in the upstream rest frame. The fluctuation in the proton number density δn , the fluctuation in the magnetic pressure δP_B , and the product of these fluctuations are presented in Figs. 4(a), 4(b), and 4(c), respectively. In Fig. 4(a), the shock front is visible as the slightly inclined horizontal discontinuity at nearly $\omega_{pe}t \sim 2 \times 10^5$ and the region below this shock front is the upstream region of the shock. Note that when the amplitude of the waves is small ($\omega_{pe}t \lesssim 1.5 \times 10^5$ in this figure), the waves propagate in the upstream ($-x$) direction, which is consistent with the explanation, which indicates that the waves are generated by the resonant mode instability. In addition, there is a positive correlation between the density fluctuation and the magnetic fluctuation. This can also be explained as a feature of the oblique mode (Gary et al. 1981). In the nonlinear regime, the waves are almost at rest in the upstream rest frame and grow in wavelength and amplitude.

3.3. Particle Acceleration

Figure 5(a) presents the energy spectra of the protons and the electrons in the downstream region of the shock at $\omega_{pe}t = 2 \times 10^5$ together with the fitted thermal Maxwellian distributions. Here, $E_{\text{kin}} = (\gamma - 1)mc^2$ denotes the kinetic energy of particles of mass m and Lorentz factor γ measured in the downstream rest frame. Note that the bulk kinetic energy of the protons and that of the electrons of the incoming plasma in the upstream region are given as approximately $2.3m_e c^2$ and approximately $7.6 \times 10^{-2}m_e c^2$, respectively. In this figure, high-energy and non-thermal populations with power-law-like distributions exist not only in protons (for $E_{\text{kin}} \gtrsim 3m_e c^2$)

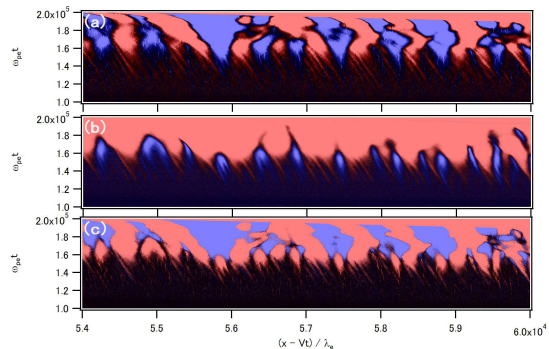


Figure 4. Evolution of upstream waves observed in the upstream rest frame. (a) Fluctuation in the proton number density δn_p . (b) Fluctuation in the magnetic pressure δP_B . (c) The product $\delta n_p \times \delta P_B$, which shows the correlation of the density fluctuation and the magnetic fluctuation. In all panels, positive values are shown in white (red), and negative values are shown in black (blue). The horizontal coordinate is $x - Vt$, where V is the upstream flow velocity measured in the simulation frame.

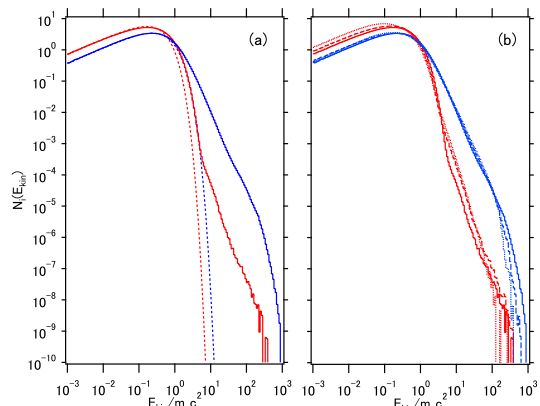


Figure 5. (a) Energy spectra of protons (black (blue) solid curve) and electrons (gray (red) solid curve) in the downstream region of the shock obtained from the simulation at $\omega_{pe}t = 2 \times 10^5$. Thermal Maxwellian distributions for protons with temperature $T_p = 0.46m_e c^2$ and for electrons with temperature $T_e = 0.24m_e c^2$ are also shown by the black (blue) dashed curve and the gray (red) dashed curve, respectively. (b) Development over time of the energy spectra. The spectra for $\omega_{pe}t = 5 \times 10^4$ (dotted curves), 1.0×10^5 (dashed curves), and 2.0×10^5 (solid curves) are shown.

but also in electrons (for $E_{\text{kin}} \gtrsim 5m_e c^2$). The power-law indices obtained from these portions of the distributions are approximately 2.4 for protons and approximately 3.0 for electrons. However, the acceleration efficiency of the electrons is clearly low compared with that of the protons. The amount of non-thermal electrons is approximately two orders of magnitude smaller than that of the non-thermal protons. Moreover, the highest energy of the electrons ($E_{\text{kin}} \sim 400m_e c^2$) is smaller than that of the protons ($E_{\text{kin}} \sim 1,000m_e c^2$).

The number densities and temperatures of the Maxwellian distributions for fitting the thermal components in Fig. 5(a) are given by $n_{p,\text{th}} = 3.3n_{e0}$ and $T_p = 0.46m_e c^2$ for protons and $n_{e,\text{th}} = 3.5n_{e0}$ and $T_e = 0.24m_e c^2$ for electrons, while the total number densities (including the non-thermal components) are given by $n_p \sim n_e \sim 4.4n_{e0}$. Here, since a fraction of the thermal electrons can be relativistic, we adopted a relativistic Maxwellian (or Jüttner-Syngé) distribution (c.f. Landau

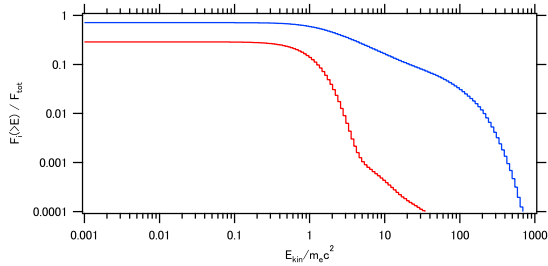


Figure 6. Cumulative energy spectra of the protons (black) and the electrons (red) in the downstream region of the shock at $\omega_{pe}t = 2 \times 10^5$ normalized by the mean total energy density.

& Lifshitz 1980). The temperature ratio $T_p/T_e \sim 1.8$ is much smaller than the mass ratio 30 indicating efficient (but not complete) energy exchange between the protons and electrons in the shock. On the other hand, the equilibrium temperature obtained if the upstream bulk kinetic energy of the plasma is fully and equally converted into the thermal kinetic energy of the protons and the electrons downstream is given by $T_{eq} = 0.79m_e c^2$. Therefore, both temperatures are lower than the equilibrium temperature. This is attributed to the fact that a fraction of energy is transferred to the non-thermal particles through the particle acceleration process. Note that the fitting by the Maxwellian distribution is not satisfactory for the electrons. This can be improved by adding a high-temperature thermal component with a temperature of approximately $0.46m_e c^2$ to the first Maxwellian component. As shown later, a fraction of the incoming electrons are accelerated in the upstream region before arriving at the shock front and these ‘pre-accelerated’ electrons would result in a high-temperature component.

Figure 5(b) shows the development over time of the energy spectra in the shock downstream region. For protons, the high-energy power-law-like portion extends over time, which is an expected behavior for the Fermi-like acceleration process with a constant injection of seed particles. However, this is not the case for electrons. The amount of non-thermal electrons decreases with time. As will be shown later, this is because the injection of the electrons to the acceleration process is not constant but rather occurs only at a particular time interval.

Figure 6 shows the cumulative energy distributions defined by

$$F_i(E) \equiv \int_E^\infty N_i(E')E'dE' \quad (1)$$

in the downstream region at $\omega_{pe}t = 2 \times 10^5$ normalized by the mean total energy density, where $i = e, p$, and $N_i(E)$ is the energy spectrum for species i shown in Fig. 5. The mean total energy density is given by $F_{tot} = F_e(0) + F_p(0)$. The total energy ratio of protons to electrons is approximately 2.5. The non-thermal protons and the non-thermal electrons contain approximately 10% and approximately 0.1%, respectively of the total particle energy downstream. These ratios are, of course, time dependent and increase as the number of non-thermal particles is increased through the acceleration process.

3.3.1. Acceleration of Protons

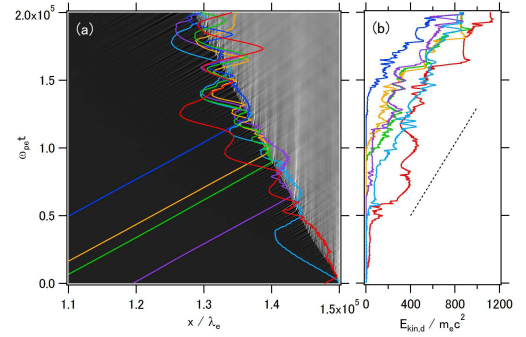


Figure 7. Acceleration histories of the highest-energy protons. The $x-t$ trajectories are shown in (a). The $E_{kin}-t$ histories are shown in (b), in which the kinetic energies E_{kin} are measured in the downstream rest frame. The dotted line denotes the case of linear acceleration at a rate of $dE_{kin}/dt \sim 7.5 \times 10^{-3}(m_e c^2 \omega_{pe})$.

Figure 7 presents the acceleration histories of the six protons that are accelerated to the highest energies in the simulation. The trajectories of these protons on the $x-t$ plane are shown in Fig. 7(a) and on the $E_{kin}-t$ plane in Fig. 7(b), where E_{kin} denotes the kinetic energy measured in the downstream rest frame. All of these protons are accelerated upon repeatedly crossing back and forth across the shock to energies up to $E_{kin} \sim 1,000 m_e c^2$. While the acceleration process is essentially a stochastic process, these protons are, on average, accelerated linearly with time. The average acceleration rate is roughly given by $dE_{kin}/dt \sim 7.5 \times 10^{-3}(m_e c^2 \omega_{pe})$, which is indicated by the dotted line in Fig. 7(b).

Figure 8 shows a representative acceleration history of the protons. In Figs. 8(a) and 8(b), the energy histories of the proton are presented on the $x_s - E_{kin}$ plane, where the kinetic energy E_{kin} is measured in the upstream rest frame in Fig. 8(a) and in the downstream rest frame in Fig. 8(b), respectively. Here, x_s is the coordinate in which the shock front is fixed at the origin $x_s = 0$ and given by $x_s(t) = x(t) - x_{sh}(t)$, where $x(t)$ is the particle position and $x_{sh}(t)$ is the shock position, both measured in the downstream rest frame. As shown in Fig. 7, the proton is accelerated by repeatedly crossing the shock. Figures 8(c) and 8(d) show the variation of the corresponding particle kinetic energies over time. Figures 8(a) through 8(d) show that the energy of the particle is almost conserved while it remains in one of the regions if the energy is measured in the plasma rest frame in that region. Therefore, the acceleration process is not a resonant process but is essentially Fermi acceleration in the sense that particles are accelerated via repeated elastic scatterings off the scattering centers at different velocities. The proton’s trajectory on the $x_s - z$ plane is shown in Fig. 8(e). The trajectory is approximately a simple gyro-orbit and is unlike that of the diffusive motion. The non-diffusive features of the acceleration process are also observed in recent simulations (Sugiyama 2011; Sironi & Spitkovsky 2011). Furthermore, there is no apparent average drift in the z -direction, namely the direction of the motional electric field, suggesting that the acceleration process is not the shock drift acceleration.

Figure 9 shows the history of the local magnetic field strength at the particle position normalized by the upstream background field, $|\mathbf{B}|/B_0$, for the same proton,

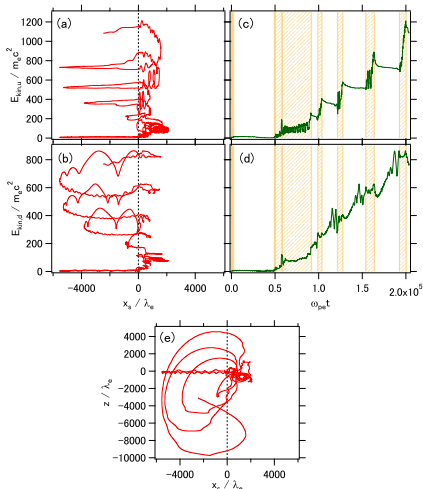


Figure 8. Representative acceleration history of protons. (a) and (b) show the acceleration history on the $x_s - E_{\text{kin}}$ plane, where x_s is the coordinate for which the shock front is fixed at the origin. The kinetic energy E_{kin} is measured in the upstream and downstream rest frames. (c) and (d) show those on the $t - E_{\text{kin}}$ plane. The shaded regions denote the time intervals in which the proton remains in the downstream region and the non-shaded regions denote the time intervals in which proton remains in the upstream region. The trajectory on the $x_s - z$ plane is shown in (e).

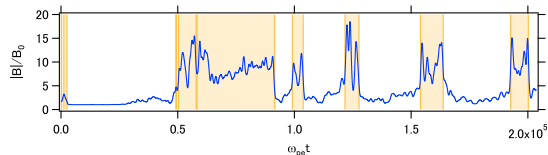


Figure 9. Local strength of magnetic field at the particle position normalized by the background field B_0 as a function of time for the same proton as in Fig. 8. The shaded regions indicate that the proton is in the downstream region.

as shown in Fig. 8. After the large-amplitude waves are well developed in the upstream region ($\omega_{\text{pet}} \gtrsim 3 \times 10^4$), the strength of the local magnetic field is at least doubled in both the upstream and downstream regions. Accordingly, the typical gyration time $\tau_B = 2\pi\omega_c^{-1}$, where $\omega_c = e|\mathbf{B}|/\gamma m_p c$ is the local proton cyclotron frequency, becomes approximately half in each region, shortening the acceleration timescale.

Figure 10(a) presents the energy gain factors per cycle of the shock crossing of the protons as a function of the energies before the shock cycle for a sample of 1,000 protons that are accelerated to energies higher than $300m_e c^2$ at $\omega_{\text{pet}} = 2 \times 10^5$. The factors are distributed around approximately 1 to 2, and for high energies they converge to approximately 1.4. The particles for which the energies more than double during a half cycle are accelerated within that region rather than upon shock crossing, although these acceleration processes are not dominant. There also exists a small fraction of particles that lose energy. Figure 10(b) shows the residence time of the particles in the upstream region and that in the downstream region for one cycle normalized by the average gyration time τ_B . Here, the average gyration time is taken over each half cycle of the shock crossing. Most of the protons return to the shock front within times on the order of the average gyration time τ_B .

For one cycle of the shock crossing of the particles,

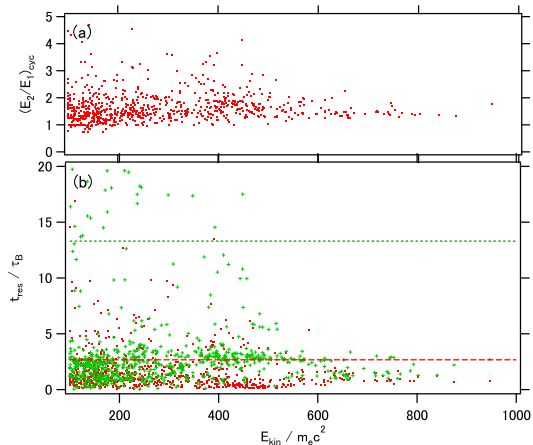


Figure 10. (a) Energy gain factor per cycle of shock crossing, E_2/E_1 , where E_1 and E_2 are the kinetic energies of the particle before and after the cycle, respectively, as a function of the kinetic energy before the crossing, $E_{\text{kin}} = E_1$, for a sample of 1,000 protons that are accelerated to energies higher than $300m_e c^2$ at the end of the simulation $\omega_{\text{pet}} = 2 \times 10^5$. (b) Residence times in the upstream region (black (red) dots) and the downstream region (gray (green) crosses) for one cycle. The residence times in the upstream and downstream regions derived from the Bohm diffusion model are also shown by the dashed and dotted lines, respectively. (See the text for details.)

the residence time until return to the shock front in each region for diffusive motion is approximately given by (cf. Kato & Takahara 2003)

$$t_{\text{res}} = \frac{4}{3} \frac{c}{|V|} \tau_0, \quad (2)$$

where τ_0 denotes the mean free time of the particle, and V is the flow speed of the scattering centers measured in the shock rest frame. If we adopt the Bohm diffusion model, the mean free time of particles is given by $\tau_0 = \tau_B$, where τ_B is the gyration time of the particle. For this model, the residence times are given by $t_{\text{res,u}} \sim 2.7\tau_B$ for the upstream region and $t_{\text{res,d}} \sim 13\tau_B$ for the downstream region. These values are indicated by the dashed and dotted lines in Fig. 10(b). Most protons return to the shock within much shorter times than those obtained from the diffusive model, while a small fraction of protons return to the shock with times that are comparable to or even longer than the diffusive time for low energies ($E_{\text{kin}} < 500$). These results confirm that the dominant acceleration process is not diffusive.

Figure 11 shows the injection properties for the same sample of protons as in Fig. 10. The energies at their first shock crossing are shown in Fig. 11(a) as a function of the first crossing time. Most of the protons are placed into the first shock cycle with the upstream bulk kinetic energy ($E_{\text{kin}} \sim 2.3m_e c^2$) without pre-acceleration. These protons will result in a constant injection of seed particles for the acceleration mechanism. On the other hand, it is also seen within some time intervals ($3 \times 10^4 < \omega_{\text{pet}} < 6 \times 10^4$, $\omega_{\text{pet}} \sim 1.2 \times 10^5$, $\omega_{\text{pet}} \sim 1.5 \times 10^5$) that the protons are pre-accelerated before the first shock crossing and gain energies up to approximately $20m_e c^2$. This would reflect the intermittent activity of the waves in the upstream region, which is also visible in Fig. 1. In Fig. 11(b), the times and the positions of the protons at which they attain energies of $E_{\text{kin}}/m_e c^2 = 5, 10, 20$, and

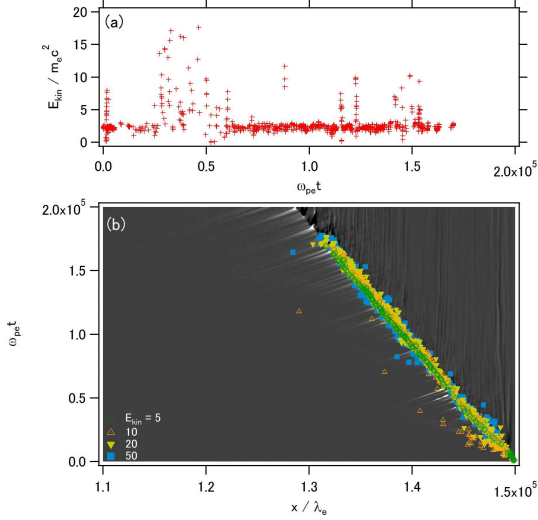


Figure 11. Injection properties for the same protons as in Fig. 10. (a) Energies of the protons at the first crossing of the shock as a function of the first crossing time. (b) Time and position when the protons attain the energies of $E_{\text{kin}}/m_e c^2 = 5, 10, 20$, and 50 for the first time.

50 for the first time are shown. We again confirm that the accelerated protons are almost constantly injected into the acceleration process at the shock front without pre-acceleration.

Figure 12 shows the phase angles of the same sample of protons as in Fig. 10 when they cross the shock front from the upstream side to the downstream side as a function of the energy at the crossing. Here, the phase angle θ is defined as the angle between the transverse component of the wave magnetic field, $\mathbf{B}_t = (0, B_y, B_z)$, at the particle position and that of the 4-velocity of the protons, $\mathbf{u}_t = (0, u_y, u_z)$, so that

$$\hat{\mathbf{B}}_t \cdot \hat{\mathbf{u}}_t = \cos \theta \quad \text{and} \quad \mathbf{n} \cdot \hat{\mathbf{u}}_t = \sin \theta, \quad (3)$$

where $\hat{\mathbf{B}}_t = \mathbf{B}_t / |\mathbf{B}_t|$, $\hat{\mathbf{u}}_t = \mathbf{u}_t / |\mathbf{u}_t|$, and $\mathbf{n} = \hat{\mathbf{x}} \times \hat{\mathbf{B}}_t$. This figure shows that, for the first shock crossings, i.e., the injection, there is a concentration of the phase angles around $\theta \sim 1.5$. This would show the phase trapping of the injected protons by the upstream large-amplitude waves (Sugiyama 1999; Sugiyama et al. 2001), suggesting that the phase trapping can play an important role in the injection process for protons. On the other hand, for later crossings or larger energies the phase angles are distributed almost uniformly, indicating that at that stage, these protons are no longer trapped by the waves and the acceleration process becomes almost independent of the phase angle.

3.3.2. Acceleration of Electrons

The acceleration process of the highest-energy electrons is shown in Figs. 13 and 14 as in Figs. 7 and 8. These electrons are accelerated by essentially the same process as that of the protons. However, there are some differences from the proton case. The acceleration process works somewhat intermittently for the electrons. Indeed, five of the six electrons shown in Fig. 13 are injected into the acceleration process around $\omega_{\text{pe}} t \sim 6 \times 10^4$. The linear acceleration rate is given by $dE_{\text{kin}}/dt \sim 1.1 \times 10^{-2} (m_e c^2 \omega_{\text{pe}})$, which is slightly larger

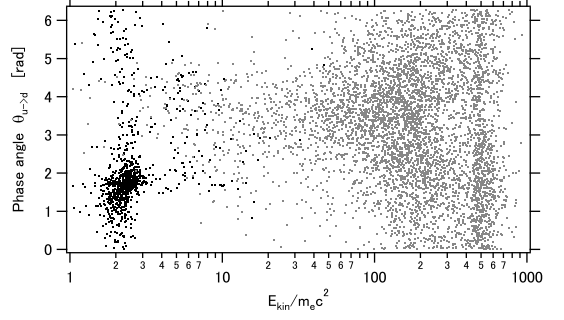


Figure 12. The angles between the transverse component of the wave magnetic field and that of the 4-velocity of the accelerated protons at the shock crossings from the upstream side to the downstream side. The sample of the protons is the same as that in Fig. 10. Those for the first shock crossing are indicated by the black dots, and the others are indicated by the gray dots as a function of their kinetic energy at the crossing.

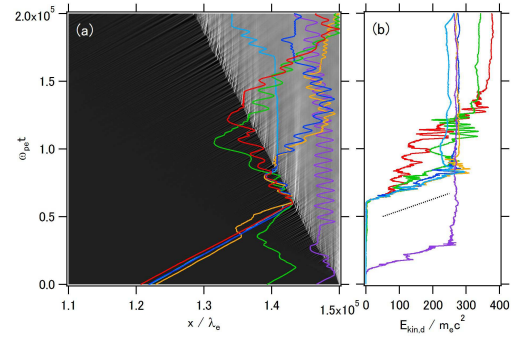


Figure 13. Acceleration histories of the highest-energy electrons as in Fig. 7. As a guide, the linear acceleration rate $dE_{\text{kin}}/dt \sim 1.1 \times 10^{-2} (m_e c^2 \omega_{\text{pe}})$ is shown by the dotted line in (b).

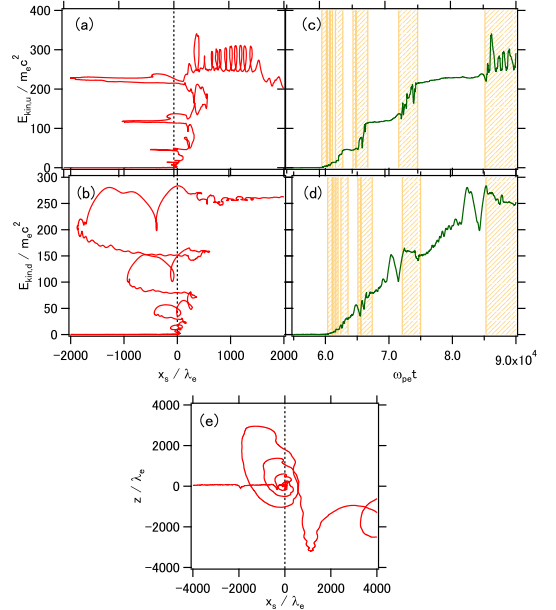


Figure 14. Representative acceleration history of electrons, as in Fig. 8.

than the case of the protons shown in Fig. 7.

Figure 15 shows the injection properties for the 321 electrons that are finally accelerated to energies higher

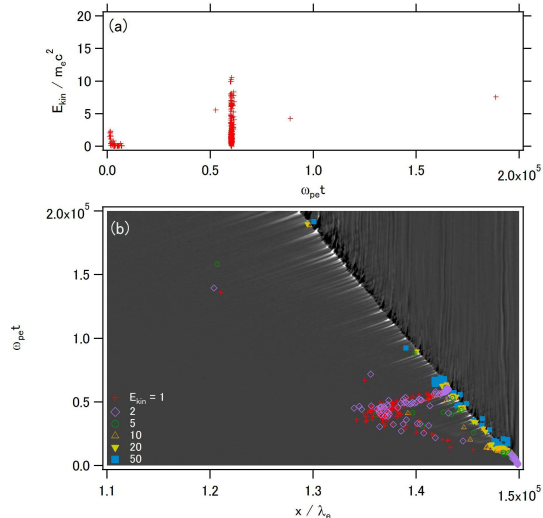


Figure 15. Injection properties for the 321 electrons that are accelerated to energies higher than $60m_e c^2$ at the end of the simulation $\omega_{pe}t = 2 \times 10^5$, as in Fig. 11. (b) Times and positions when the electrons attain the energies of $E_{kin}/m_e c^2 = 1, 2, 5, 10, 20,$ and 50 for the first time.

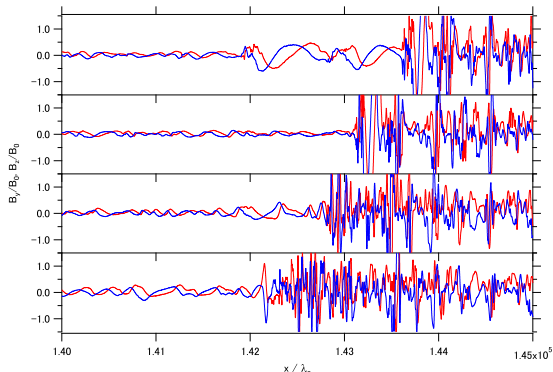


Figure 16. Evolution of the upstream waves around $\omega_{pe}t = 6 \times 10^4$. The components B_y (in black (red)) and B_z (in gray (blue)) are shown from top to bottom for $\omega_{pe}t = 5.5 \times 10^4, 6 \times 10^4, 6.5 \times 10^4,$ and 7×10^4 .

than $60m_e c^2$, as in Fig. 11. In contrast to the case in which the protons are injected into the acceleration process at an approximately constant rate, almost all of the electrons are injected around $\omega_{pe}t \sim 6 \times 10^4$, with some exceptions. The energies at the first shock crossing are much higher than the upstream bulk kinetic energy of the electrons (approximately $0.076m_e c^2$), indicating a pre-acceleration in the upstream region. The time of the efficient injection coincides with the end of the time interval observed in the proton injection in which the pre-acceleration of protons is efficient (see Fig. 11(a)). During this time interval, the amplitudes of the upstream waves become very low (see Fig. 16). On the other hand, just before that time, the wave amplitude grows to very high level. The injection efficiency of both protons and electrons would be related with these wave activities.

The injection properties for the 1,000 sample electrons that achieve slightly lower energies $50 < E_{kin}/m_e c^2 < 60$ at the end of the simulation is shown in Fig. 17, as in Fig. 15. In this case, the electrons are injected into the acceleration process even at other times. The electrons

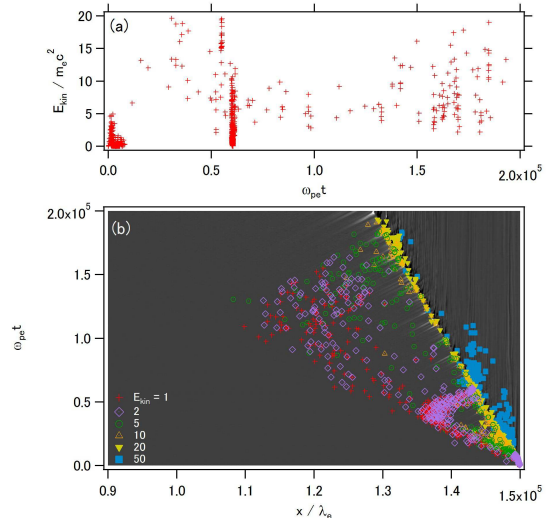


Figure 17. Same as Fig. 15, but for the 1,000 electrons accelerated to energies within the range of between $50m_e c^2$ and $60m_e c^2$ at $\omega_{pe}t = 2 \times 10^5$.

are pre-accelerated in a part of the upstream region and the width of this region is extended with time, as shown in Fig. 17(b). This region coincides with the foreshock region, where large-amplitude waves exist (see Fig. 1). With this extension of the pre-acceleration region, the typical energies at the first shock crossing are also increasing, as shown in Fig. 17(a) for $\omega_{pe}t > 1 \times 10^5$. In particular, for $\omega_{pe}t > 1.5 \times 10^5$, approximately half of the injected electrons have gained energy in the upstream region to higher than $10m_e c^2$ before the electrons reach the shock front. Although these pre-accelerated electrons have not contributed to the highest-energy electrons shown in Fig. 15 by the end of the simulation, they may contribute at a later time.

Figure 18 shows the energy spectra of the electrons calculated for three regions upstream of the shock at $\omega_{pe}t = 1 \times 10^5$. The bulk upstream electrons are heated by advection as they approach the shock. Their energy spectra in each region are well fitted by Maxwellian distributions. Moreover, a fraction of electrons are accelerated to high energies in the foreshock region, where the amplitude of the upstream waves becomes large, as shown in Fig. 17. This component can also be fitted by a Maxwellian although its temperature (approximately $0.35m_e c^2$) is much higher than that of the bulk electrons. As already mentioned, these pre-accelerated electrons would result in the high-temperature Maxwellian component in the downstream region. These pre-acceleration processes may later contribute to the steady electron injection for the Fermi-like acceleration process.

4. DISCUSSION

In the present simulation of a quasi-parallel shock, we observed ion (proton) acceleration and the associated wave generation around the shock. Such processes are also observed in quasi-parallel shocks in the heliosphere by *in situ* observations with spacecraft. In particular, the ion acceleration is observed in, for example, the Earth's bow shock (Burgess et al. 2012) and the shocks associated with the solar energetic particle events (Lee et al. 2012). For the latter, the ion energy spectrum shows a

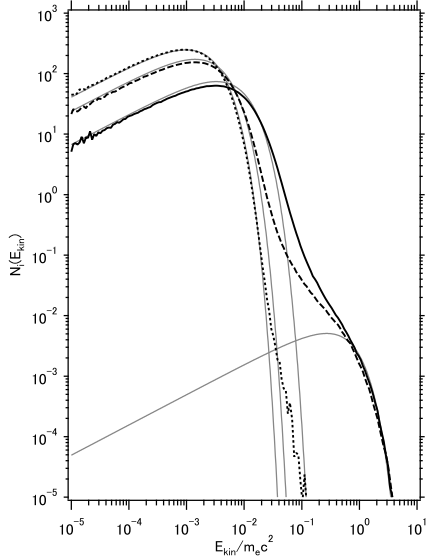


Figure 18. Electron energy spectra in three upstream regions at $\omega_{pe}t = 1 \times 10^5$, where the shock is located at $x \sim 1.39 \times 10^5 \lambda_e$ and the energies are measured in the upstream rest frame. Electron energy spectra obtained for the regions of $9 \times 10^4 < x/\lambda_e < 9.5 \times 10^4$ (dotted curve), $1.1 \times 10^5 < x/\lambda_e < 1.15 \times 10^5$ (dashed curve), and $1.3 \times 10^5 < x/\lambda_e < 1.35 \times 10^5$ (solid curve) are shown in black. The curves in gray show the fitted relativistic Maxwellians with temperatures of $T/m_e c^2 = 0.0020$ (which is the far upstream temperature), 0.0028, 0.0065, and 0.35.

power-law shape and considered to be accelerated by the diffusive first-order Fermi acceleration mechanism. On the other hand, in the present simulation, as shown in Section 3.3.1, the dominant acceleration mechanism are not diffusive but a process that has a shorter acceleration timescale, which is similar to the “scatter-free” acceleration mechanism (Sugiyama et al. 2001; Sugiyama 2011). Regardless of the difference in the dominant acceleration mechanism, the resulting energy spectrum still becomes a power-law shape. The reason would be that it still satisfies the fundamental requirements for the Fermi-type acceleration mechanism, i.e., the repeated shock crossings, the elastic scattering in the scattering center rest frame, and an approximately constant escape probability from the acceleration cycle, although the spatial motion of the particles is not diffusive. The large-amplitude upstream waves observed in the simulation have a similar structure to the ULF waves observed in the quasi-parallel Earth’s bow shock by *in situ* observation (Hoppe et al. 1981); in the present simulation, the reflected/accelerated protons would play a similar role to the energetic diffuse ions in Earth’s bow shock for generating these waves. The somewhat regular perpendicular magnetic structure due to the generated waves in the upstream region observed in the simulation may be caused by the 1D dimensionality of the simulation. In fact, recent multi-dimensional hybrid simulations of high-Mach-number quasi-parallel shocks show more turbulent magnetic structures around the shock transition region (Caprioli & Spitkovsky 2014). To see whether the 1D dimensionality affects the results significantly, some multi-dimensional simulations are desired.

Amano & Hoshino (2010) proposed an electron injection model with a critical Alfvén Mach number above which the electron injection occurs. From observations in

the heliosphere, it seems that this criterion is satisfied in several shocks in which electron acceleration is observed (e.g., Oka et al. 2006; Masters et al. 2013). It would be worthwhile to see whether this electron injection mechanism operated in the present simulation. The electron acceleration occurred only around $\omega_{pe}t \sim 6 \times 10^4$ in the simulation. In this time interval, the amplitude of the upstream waves is temporally reduced as shown in Fig. 16 and the local inclination angle of the magnetic field at just upstream of the shock is given by $\Theta \sim 30^\circ - 60^\circ$. The critical Mach number is thus given by $M_A^{\text{inj}} = 0.8 - 1.5$. On the other hand, the local Alfvén Mach number is only slightly reduced from the global value of $M_A = 28$. Hence, the condition for injection $M_A \gg M_A^{\text{inj}}$ is satisfied and, from the criterion argument, the electron injection is expected to occur. In their injection model, it is assumed that a fraction of the incoming electrons are reflected at the shock front to form the electron beam and then generate the whistler waves in the upstream region, and finally these waves scatter the electrons leading to the diffusive acceleration. Thus, we seek such electron beams reflected at the shock front in the phase-space plots at $\omega_{pe}t = 4 \times 10^4$, 5×10^4 , and 6×10^4 . However, such beams couldn’t be found. In addition, the trajectories of the accelerated electrons show no clear indication of the interaction with the whistler waves. Therefore, it seems that the injection mechanism of the electrons observed in the simulation is different from those considered in Amano & Hoshino (2010). On the other hand, in the other times, their injection mechanism does not operate, too, although the criterion is still satisfied, where the local inclination angle of the magnetic field is typically given by $\Theta \sim 80^\circ$ and the critical Mach number becomes $M_A^{\text{inj}} < 1$. Regarding this point, it should be noted that in the present simulation the superluminal condition can be realized because the shock velocity is relatively large ($\sim 0.46c$) and also the local inclination angle of the magnetic field becomes quasi-perpendicular after the upstream waves grow substantially; the condition for the shock to be subluminal is $\Theta < 63^\circ$ for $V_s = 0.46c$ and this is difficult to be satisfied after the upstream waves grow to large amplitude. In such cases, the de Hoffmann-Teller frame does not exist and so the incoming electrons cannot be reflected at the shock front. Thus, to see whether the electron reflection at the shock front occurs and the injection process proposed by Amano & Hoshino (2010) operates, simulations with smaller shock velocities would be needed. This should be investigated in the future studies.

In Section 3.1, the local shock structure becomes substantially quasi-perpendicular after the amplitude of the upstream waves grow to be sufficiently large. This would be a common feature of the quasi-parallel shocks in which the particle acceleration is efficient and the accelerated particles excite large-amplitude waves in the upstream region. In such local quasi-perpendicular conditions, as observed in several simulations of the perpendicular shocks (Amano & Hoshino 2009; Kato & Takabe 2010; Sironi & Spitkovsky 2011; Riquelme & Spitkovsky 2011; Matsumoto et al. 2013), the electron heating and/or acceleration in the foot region of the shock structure can also occur (depending on the shock parameters and the dimensionality of the simulation) in addition to the elec-

tron acceleration/heating in the upstream wave region found in Section 3.3.2. Regarding this shock structure, while we observe that the shock is simply formed in the environment of the local quasi-perpendicular magnetic field, the shock formation due to the nonlinear steepening of the upstream waves themselves was also reported for relativistic parallel shocks (Sironi & Spitkovsky 2011). This would indicate that the shock structure can depend on the shock speed. Which shock structure is realized would be determined by whether the typical gyro-radius of the protons reflected at the shock front is larger than the typical wavelength of the upstream waves.

Note that, for PIC simulations, in particular those dealing with the particle acceleration process, as in the present work, the number of super-particles used in the simulations can be important because high-energy particles in the simulations generally suffer from the energy loss process due to the stopping power of the plasma (Kato 2013). The energy loss rate is inversely proportional to the number of super-particles in the electron skin depth volume, N_e . Therefore, if N_e is too small, the energy loss process becomes significant making the acceleration process inefficient. For one-dimensional simulations, the energy loss rate for relativistic particles is given by

$$\frac{dE_{\text{kin}}}{dt} \sim -\frac{1}{2N_e}(m_e c^2 \omega_{pe}). \quad (4)$$

From Figs 7 and 13, if we take the representative value of the acceleration rate for the present case to be $dE_{\text{kin}}/dt \sim 1 \times 10^{-2}(m_e c^2 \omega_{pe})$, the value of N_e for which the energy loss rate is equal to the acceleration rate, is given by $N_e \sim 50$. Figure 19 shows the energy spectra of protons and electrons in the shock downstream region at $\omega_{pe}t = 2 \times 10^5$, as in Fig. 5(a), for four simulations that are identical except for the value of N_e . The acceleration efficiency is indeed dependent on N_e for both protons and electrons. In particular, in the case of $N_e = 50$ (in which the number of super-particles per cell is $N_{\text{PPC}} = 3$ for $\Delta x = 0.06\lambda_e$) and $N_e = 133$ ($N_{\text{PPC}} = 8$), the acceleration process becomes significantly inefficient and is almost completely nonfunctional. Even in the case of $N_e = 667$ ($N_{\text{PPC}} = 40$), the acceleration efficiency is still affected by the energy loss. Thus, for these simulations, the number of super-particles used should be chosen to be sufficiently large, so that the energy loss is negligible.

In the present paper, we observed that electron injection occurs only within a particular time interval ($\omega_{pe}t \sim 6 \times 10^4$) and does not settle at a constant rate, at least during the calculation time of the simulation. For longer timescales, the electron injection would be able to occur constantly or repeatedly. Instead, the electron injection observed in the simulation may be a consequence of the initial condition and may not occur again. In order to resolve this issue, further long-term simulations are required. In addition, in two or three dimensions, some electromagnetic instabilities, such as the ion-Weibel instability, can play important roles, even for non-relativistic shocks (Kato & Takabe 2008; Niemiec et al. 2012), and these effects can influence the particle acceleration process and the shock structure. Thus, multi-dimensional and long-term PIC simulations are also desired.

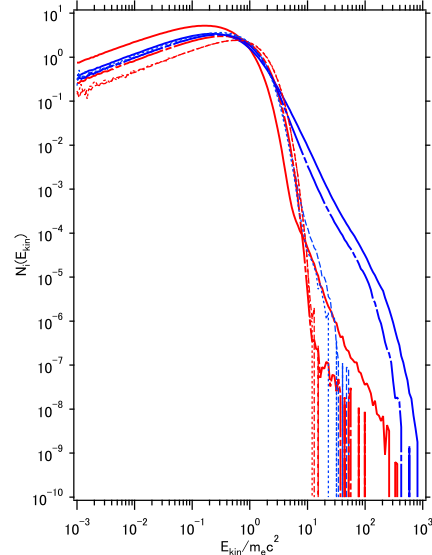


Figure 19. Energy spectra in the downstream region of the shock at $\omega_{pe}t = 2 \times 10^5$ for protons (in black (blue)) and electrons (in gray (red)), as in Fig. 5, for four simulations that are identical except for the number of super-particles within the electron skin depth, N_e : $N_e = 50$ (dotted curves), $N_e = 133$ (dashed curves), $N_e = 667$ (dot-dashed curves), and $N_e = 2,667$ (solid curves), for which the results are shown in Section 3.

5. CONCLUSION

We have carried out a long-term, large-scale PIC simulation of a quasi-parallel high-Mach-number shock in an electron-proton plasma. We showed that both protons and electrons are accelerated in the shock, and these accelerated particles generate large-amplitude Alfvénic waves in the upstream region of the shock. The local structure of the collisionless shock becomes substantially similar to that of the quasi-perpendicular shocks because the transverse components of the incident upstream waves dominates the parallel background field. A fraction of the protons are accelerated in the shock with a power-law-like energy distribution as has been demonstrated through several hybrid simulations. The injection process for the protons operates almost constantly. In the process, phase trapping of the protons by upstream waves can play an important role, while the later acceleration process is nearly independent of the phase angle. The dominant acceleration process is a Fermi-like process that occurs through repeated shock crossings of the protons but is not diffusive. Most of the accelerated protons complete one-cycle of the acceleration process within a time on the order of the gyration time, which is much shorter than the diffusion time. We also found that electrons are accelerated in the shock by the same mechanism, and the energy spectrum of the accelerated electrons has a power-law like distribution. However, the injection is not constant, and electrons are actually injected during only one time interval in the simulation. This behavior would be related to the intermittent activity of the upstream waves. Upstream of the shock, a fraction of the electrons is accelerated before reaching the shock, which would result in a two-temperature electron distribution in the downstream region. At a later time, the pre-acceleration process may contribute to steady electron injection for the Fermi-like acceleration process.

We would like to thank the anonymous referee for the valuable comments. This work was supported by JSPS KAKENHI Grant Number 22740164, 24540277. Numerical computations were carried out on Cray XC30 at Center for Computational Astrophysics, National Astronomical Observatory of Japan.

REFERENCES

- Ackermann, M. et al. 2013, *Science*, 339, 807
 Amano, T., & Hoshino, M. 2009, *ApJ*, 690, 244
 Amano, T., & Hoshino, M. 2010, *Phys. Rev. Lett.*, 104, 181102
 Bamba, A., Yamazaki, R., Ueno, M., & Koyama, K. 2003, *ApJ*, 589, 827
 Bell, A. R. 1978, *MNRAS*, 182, 147
 Birdsall, C. K., & Langdon, A. B. 1991, *Plasma Physics via Computer Simulation* (Bristol: IOP)
 Blandford, R. D., & Eichler, D. 1987, *Phys. Rep.*, 154, 1
 Burgess D., Lucek E. A., Scholer M., et al. 2005, *Space Sci. Rev.*, 118, 205
 Burgess D., M'obius E., & Scholer M. 2012, *Space Sci. Rev.*, 173, 5
 Caprioli, D., & Spitkovsky, A. 2014, *ApJ*, 783, 91
 Drury, L.O.C. 1983, *Rep. Prog. Phys.*, 46, 973
 Gargaté, L., & Spitkovsky, A. 2012, *ApJ*, 744, 67
 Gary, S. P., Gosling, J. T., & Forslund, D. W. 1981, *J. Geophys. Res.*, 86, 6691
 Giacalone, J. 2004, *ApJ*, 609, 452
 Hoppe, M. M., Russel, C. T., Frank, L. A., Eastman, T. E., & FGreenstadt, E. W. 1981, *J. Geophys. Res.*, 86, 4471
 Kato, T. N. 2013, arXiv:1312.5507
 Kato, T. N. & Takabe, H. 2008, *ApJ*, 681, L93
 Kato, T. N. & Takabe, H. 2010, *ApJ*, 721, 828
 Kato, T. N. & Takahara, F. 2003, *MNRAS*, 342, 639
 Koyama, K., Petre, R., Gotthelf, E. V., et al. 1995, *Nature*, 378, 255
 Landau, L. D. & Lifshitz, E. M. 1980, *Statistical Physics*, 3rd Edition Part 1 (Oxford : Butterworth-Heinemann)
 Lee M. A., Mewaldt R. A., & Giacalone J. 2012, *Space Sci. Rev.*, 173, 247
 Long, K. S., Reynolds, S. P., Raymond, J. C., et al. 2003, *ApJ*, 586, 1162
 Masters A., Stawarz L., Fujimoto M., et al. 2013, *Nature phys.*, 9, 164
 Matsumoto, Y., Amano, T. & Hoshino, M. 2013, *Phys. Rev. Lett.*, 111, 215003
 Niemiec, J., Pohl, M., Bret, A., & Wieland, V. 2012, *ApJ*, 759, 73
 Oka M., Terasawa T., Seki Y., et al. 2006, *Geophys. Res. Lett.*, 33, L24104
 Reames, D. V. 2000, *AIP Conf. Proc.*, 516, 289
 Reynoso, E. M., Hughes J. P. & Moffett D. A. 2013, *ApJ*, 145, 104
 Riquelme, M. A., & Spitkovsky, A. 2011, *ApJ*, 733, 63
 Sironi, L., & Spitkovsky, A. 2011, *ApJ*, 726, 75
 Sugiyama, T. 2011, *Phys. Plasmas*, 18, 022302
 Sugiyama, T., Fujimoto, M., & Mukai, T. 2001, *J. Geophys. Res.*, 106, 21657
 Sugiyama, T., & Terasawa, T. 1999, *Adv. Space Res.*, 24, 73
 Winske, D., & Leroy, M. M. 1984, *J. Geophys. Res.*, 89, 2673